Identifying possible pairing states in Sr_{2}RuO_{4} by tunneling spectroscopy

Shu-Ichiro Suzuki, Masatoshi Sato, and Yukio Tanaka

Phys. Rev. B **101**, 054505 — Published 12 February 2020

DOI: 10.1103/PhysRevB.101.054505

Identifying possible pairing states in Sr_2RuO_4 by tunneling spectroscopy

Shu-Ichiro Suzuki[1], Masatoshi Sato[2], and Yukio Tanaka[1]
[1] *Department of Applied Physics, Nagoya University, Nagoya 464-8603, Japan and*
[2] *Yukawa Institute for Theoretical Physics, Kyoto University, Kyoto 606-8502, Japan*
(Dated: January 27, 2020)

We examine the tunneling spectroscopy of three-dimensional normal-metal/Sr_2RuO_4 junctions as an experimental means to identify pairing symmetry in Sr_2RuO_4. In particular, we consider three different possible pairing states in Sr_2RuO_4: spin-singlet chiral d-wave, spin-triplet helical p-wave, and spin-nematic f-wave ones, all of which are consistent with recent nuclear-magnetic-resonance experiments [A. Pustogow *et al.*, Nature **574**, 72 (2019)]. The Blonder-Tinkham-Klapwijk theory is employed to calculate the tunneling conductance, and the cylindrical two-dimensional Fermi surface of Sr_2RuO_4 is properly taken into account as an anisotropic effective mass and a cutoff in the momentum integration. It is pointed out that the chiral d-wave pairing state is inconsistent with previous tunneling conductance experiments along the c-axis. We also find that the remaining candidates, the spin-triplet helical p-wave pairing state and the spin-nematic f-wave ones, can be distinguished from each other by the in-plane tunneling spectroscopy along the a- and b-axes.

I. INTRODUCTION

The pairing symmetry of Sr_2RuO_4 has been a mystery since its discovery[1–3]. Until recently, the most promising candidate had been the chiral p-wave (i.e., $p_x + ip_y$-wave) pairing[4], which is spin-triplet with broken time-reversal symmetry (TRS). The spin-triplet pairing was widely accepted since it is consistent with a variety of experiments such as polarized-neutron-scatterings[5], half-quantum vortices[6,7], the transport measurements[8–15], and in particular the nuclear-magnetic-resonance (NMR) measurement[16]. There were also a number of theoretical studies supporting the spin-triplet scenario[17–24]. However, the situation has been changed after a recent report[25] pointing out an over-heating problem in the previous NMR measurements. The new NMR data without the heating problem show the reduction of the in-plane spin susceptibility[25,26] below T_c, which conflicts with the in-plane equal spin structure of the chiral p-wave pairing where the d-vector is pinned along the c-axis. Moreover, a first-order phase transition of the superconducting state triggered by an in-plane magnetic field[27–29] also suggests a different spin structure.

In addition to the spin structure, TRS in the superconducting state has been controversial. The spontaneous TRS breaking has been reported by the muon-spin-relaxation (μSR) and the Kerr-effect measurements[30,31]. The ultrasound measurements[32,33] also suggest a two-dimensional (2D) gap function, which is also consistent with broken TRS. In contrast, the spontaneous edge current associated with a chiral state has never been observed so far[34–42]. A recent report on the Josephson effects also supports the presence of TRS[43,44]. Moreover, two different nodal structures of the superconducting gap have been reported. The thermal-conductivity[45] and specific-heat measurements[46] suggest a vertical and horizontal line node (or gap minimum), respectively.

Two alternative pairing states have been proposed to explain the Knight-shift measurements[25,26], together with a part of the other experiments. One is a chiral d-wave (i.e., $d_{zx}+id_{yz}$-wave) pairing[47], which is spin-singlet with broken TRS and a horizontal line node. The other is a helical p-wave pairing state that preserves TRS and may reproduce the in-plane transport measurements[9]. The latter pairing is an one-dimensional irreducible representation and has no node on the Fermi surface (FS).

We also would like to point out here that spin-nematic pairings could be consistent with several experiments including the recent NMR data: They are spin-triplet and compatible with the NMR experiments if their d-vector points to the direction of the applied magnetic fields (i.e., the a-axis). They can also be consistent with the ultrasound measurements and the Josephson effects since the spin-nematic pairings are multi-dimensional with TRS. Moreover, a spin-nematic f_{xyz}-wave pairing [see Eq. (9)] can reproduce the four-fold symmetric superconducting gap with horizontal and line nodes.

Although these pairing states are not fully consistent with all of the existing experiments, all of them may reproduce the NMR Knight-shift measurements. Obviously, a solid experimental means that can distinguish the above pairings is highly desired.

A remarkable property of unconventional superconductors (SCs) including Sr_2RuO_4 is the presence of surface Andreev bound states[48] (ABSs). The bound states are formed at a boundary of an SC when the phases of the pair potential for incoming and outgoing quasiparticles

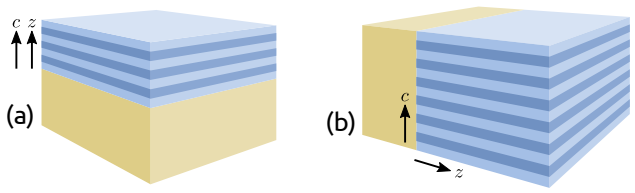

FIG. 1. Schematics of the three-dimensional junctions. The stripes represent the layers of RuO_2 planes. The c-axis of Sr_2RuO_4 is (a) parallel and (b) perpendicular to the interface normal.

are different.[49–57] Their energy dispersion reflects the internal phase of the anisotropic pairing, and manifests as a zero-energy peak (ZEP) in the conductance spectra. A sharp ZEP appears when the ABSs form a flat band, while a dome-shaped broad ZEP arises when the ABSs are dispersive[12,50–52]. Comparing the conductance spectra in details, one can obtain the information of the pair potential with which the above three pairing states can be distinguished.

In this paper, we propose the tunneling spectroscopy of three-dimensional normal-metal/Sr_2RuO_4 junctions as an experimental means to determine the pairing symmetry of Sr_2RuO_4. We examine three-dimensional junctions as shown in Fig. 1 where the cylindrical FS of Sr_2RuO_4 (see Fig. 2) is taken into account. We consider the spin-singlet $d_{zx}+id_{yz}$-wave, spin-nematic f_{xyz}-wave, and spin-triplet helical p-wave pairing states. It is shown that the $d_{zx}+id_{yz}$-wave pairing state hosts a sharp robust ZEP at the (001) surface. Comparing it with the spectroscopy data by the scanning tunneling microscope (STM)[58–60], we exclude the $d_{zx}+id_{yz}$ pairing from possible pairings of Sr_2RuO_4. Even though a simple spin nematic f_{xyz}-wave pairing has a similar ZEP at the (001) surface, this peak is fragile and easily suppressed by, for example, the Rashba spin-orbit interaction (RSOI) at the interface. Thus, the spin-nematic state could be consistent with the STM data. Then the spin-triplet helical p-wave pairing naturally reproduces the STM data. The latter two pairings, spin-triplet f_{xyz}-wave and helical p-wave pairings, can be distinguished by the conductance spectra of the (100)- and (110)-interface junctions. For the f_{xyz}-wave junctions, the conductance spectra are different between these junctions: the ZEP appears in the (100) case but a V-shaped spectrum dose in the (110) case. In contrast, those for the helical p-wave SC are qualitatively identical.

II. BLONDER-TINKHAM-KLAPWIJK THEORY

In this paper, we consider three-dimensional junctions as shown in Fig. 1. A normal metal (N) and an SC occupy $z<0$ and $z\geq 0$, respectively. The junction is assumed infinitely large in the x and y directions. The interface normal vector $\boldsymbol{e}_z$ is perpendicular or parallel to the c axis of Sr_2RuO_4 as shown in Figs. 1(a) and 1(b), respectively.

The Hamiltonian for superconducting systems is given by

$$\mathcal{H}=\frac{1}{2}\int \Psi^\dagger(\boldsymbol{r})\check{H}_B(\boldsymbol{r})\Psi(\boldsymbol{r})\,d\boldsymbol{r}, \tag{1}$$

$$\Psi(\boldsymbol{r})=[\ \psi_\uparrow(\boldsymbol{r})\ \ \psi_\downarrow(\boldsymbol{r})\ \ \psi^\dagger_\uparrow(\boldsymbol{r})\ \ \psi^\dagger_\downarrow(\boldsymbol{r})\ ]^T, \tag{2}$$

with the Bogoliubov-de Gennes (BdG) Hamiltonian

$$\check{H}_B(\boldsymbol{r})=\begin{bmatrix}\hat{h}(\boldsymbol{r}) & \hat{\Delta}(\boldsymbol{r})\\ -\hat{\Delta}^*(\boldsymbol{r}) & -\hat{h}^*(\boldsymbol{r})\end{bmatrix}, \tag{3}$$

$$\hat{\Delta}(\boldsymbol{r})=i\left[d_0(\boldsymbol{r})+\boldsymbol{d}(\boldsymbol{r})\cdot\hat{\boldsymbol{\sigma}}\right]\hat{\sigma}_y\Theta(z), \tag{4}$$

where d_0 and $\boldsymbol{d}$ are the spin-singlet and spin-triplet components of the pair potential, $\hat{\sigma}_0$ and $\hat{\sigma}_\nu$ $(\nu=x,y,z)$ are the identity and the Pauli matrices in the spin space, and T being the transpose of a matrix. Throughout this paper, the symbol $\hat{\cdot}$ ($\check{\cdot}$) represents a 2×2 (4×4) matrix in the spin (spin-Nambu) space.

The single-particle Hamiltonian $\hat{h}(\boldsymbol{r})=\hat{h}_{\rm SP}+\hat{h}_{\rm SO}+\hat{h}_{\rm B}$ is

$$\hat{h}_{\rm SP}=\left[-\frac{\hbar^2}{2}\sum_\nu\frac{1}{m_\nu}\frac{\partial^2}{\partial\nu^2}-\mu_F\right]\hat{\sigma}_0, \tag{5}$$

$$\hat{h}_{\rm SO}=V_{\rm SO}\delta(z)\boldsymbol{e}_z\cdot[\boldsymbol{p}\times\hat{\boldsymbol{\sigma}}],\quad \hat{h}_{\rm B}=V_{\rm B}\delta(z)\hat{\sigma}_0, \tag{6}$$

where $\hat{h}_{\rm SO}$ and $\hat{h}_{\rm B}$ represent the Rashba spin-orbit interaction (RSOI) and the potential barrier at the interface and m_ν are the effective mass in the ν direction. The Fermi surface of the SC and the N is uniaxially anisotropic and isotropic respectively. Introducing the anisotropic effective mass, one can model anisotropic FSs. Their effective masses are given by

$$(m_a,m_b,m_c)=\begin{cases}(m_N,m_N,m_N) & \text{for } x<0,\\ (m_\parallel,m_\parallel,m_\perp) & \text{for } x\geq 0.\end{cases} \tag{7}$$

These assumptions are valid for layered superconducting materials such as Sr_2RuO_4.

In this paper, we consider four types of pair potentials: (1) spin-singlet $d_{zx}+id_{yz}$-wave, (2) spin-triplet f-wave, (3) spin-triplet helical p-wave, and (4) spin-singlet s-wave. Each pair potential is given by

$$(1)\ d_0=\bar{\Delta}_0(\partial_c\partial_a+i\partial_b\partial_c)/k_\parallel^S k_\perp^S, \tag{8}$$

$$(2)\ \boldsymbol{d}=\boldsymbol{e}_a(\bar{\Delta}_0\partial_a\partial_b\partial_c)/(k_\parallel^S)^2k_\perp^S, \tag{9}$$

$$(3)\ \boldsymbol{d}=\bar{\Delta}_0(\boldsymbol{e}_a\partial_a+\boldsymbol{e}_b\partial_b)/k_\parallel^S, \tag{10}$$

$$(4)\ d_0=\bar{\Delta}_0, \tag{11}$$

where $\bar{\Delta}_0$ is determined so that $\max[d_{\boldsymbol{k}}]=\Delta_0$ on the FS with $d_{\boldsymbol{k}}=\sqrt{d_0^2+|\boldsymbol{d}|^2}$ and $\Delta_0\in\mathbb{R}$ characterizes the amplitude of the pair potential, and $k_{s\parallel}$ and $k_{s\perp}$ are the Fermi momentum parallel and perpendicular to the k_a-k_b plane in the superconductor. The d-vector of the spin-nematic f-wave pairing is assumed parallel to the a-axis. This d-vector reproduces the NMR results[25,26], where an external magnetic field is applied in the [100] direction. This anisotropic d-vector reduces the four-fold rotational symmetry stemming from the crystal structure into two-fold one (i.e., spin-nematic superconductivity). The spin-nematic f-wave pairings with $\boldsymbol{d}\parallel\boldsymbol{a}$ and $\boldsymbol{d}\parallel\boldsymbol{b}$ are degenerated. In this paper, we refer to each pair potential as (1) chiral d-wave (chiral DW), (2) spin-nematic f-wave (spin-nematic FW), (3) helical p-wave (helical PW), and (4) s-wave (SW) SC. The SW, helical PW, and spin-nematic FW pairings are time-reversal symmetric, whereas the the chiral DW one breaks TRS.

From the experimental data obtained so far, we cannot exclude the possibility of the existence of subdomi-

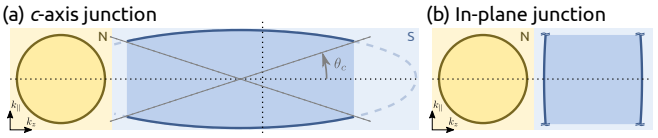

FIG. 2. Schematics of the Fermi surfaces. The FS of the SC is anisotropic due to the anisotropic effective mass. The cut-off angle θ_c is introduced to make the FS in the SC cylindrical which is important when we estimate the effects of the Rashba spin-orbit coupling.

nant pair potentials for the FW pairing where the subdominant component should also belong to the 2D irreducible representation[61]. Such a subdominant component changes the node to a small minimum and can gain the condensation energy. Therefore, to discuss the effects of a subdominant component, we introduce the parameters η_a and η_b with which the d-vector is given by

$$\boldsymbol{d} = \bar{\Delta}_0 \boldsymbol{e}_a (k_a k_b k_c) + \eta_a \Delta_0 \boldsymbol{e}_c k_a + \eta_b \Delta_0 \boldsymbol{e}_c k_b, \tag{12}$$

where, we consider the subdominant components linear function of the momentum (i.e., p_x- and p_y-wave pairing as subdominant components with $\boldsymbol{d} \parallel \boldsymbol{c}$).

The wave functions obey the Bogoliubov-de Gennes (BdG) equation: $\check{H}\Psi = E\Psi$. In the present case, the momenta parallel to the interface k_x and k_y are good quantum numbers because of translational symmetry. Therefore, the BdG equation is decomposed as

$$\check{H}_{\boldsymbol{k}_\parallel} \Psi_{\boldsymbol{k}_\parallel}(z) = E_{\boldsymbol{k}_\parallel} \Psi_{\boldsymbol{k}_\parallel}(z) \tag{13}$$

$$\check{H}_{\boldsymbol{k}_\parallel}(z) = \begin{bmatrix} \hat{h}_{\boldsymbol{k}_\parallel}(z) & \hat{\Delta}_{\boldsymbol{k}_\parallel}(z) \\ -\hat{\Delta}^*_{-\boldsymbol{k}_\parallel}(z) & -\hat{h}^*_{-\boldsymbol{k}_\parallel}(z) \end{bmatrix}, \tag{14}$$

$$\Psi(\boldsymbol{r}) = \sum_{\boldsymbol{k}_\parallel} \Psi_{\boldsymbol{k}_\parallel}(z) \frac{e^{i(k_x x + k_y y)}}{\sqrt{L_x L_y}}, \tag{15}$$

$$\Psi_{\boldsymbol{k}_\parallel}(z) = [\ \psi_{\uparrow,\boldsymbol{k}_\parallel} \quad \psi_{\downarrow,\boldsymbol{k}_\parallel} \quad \psi^\dagger_{\uparrow,-\boldsymbol{k}_\parallel} \quad \psi^\dagger_{\downarrow,-\boldsymbol{k}_\parallel}\ ]^T, \tag{16}$$

where $\boldsymbol{k}_\parallel = (k_x, k_y, 0)$. The normal part of $\check{H}_{\boldsymbol{k}_\parallel}$ is given by

$$\hat{h}_{\boldsymbol{k}_\parallel} = \left[-\frac{\hbar^2}{2m_z} \partial z^2 - \mu_{\boldsymbol{k}_\parallel} \right] \hat{\sigma}_0 + \hat{V}\delta(z) \tag{17}$$

$$\mu_{\boldsymbol{k}_\parallel} = \mu_F + \hbar^2 k_x^2 / 2m_x + \hbar^2 k_y^2 / 2m_y, \tag{18}$$

$$\hat{V} = V_{\rm B} \check{\sigma}_0 + V_{\rm SO} \hat{\Lambda}, \tag{19}$$

where $\hat{\Lambda} = \boldsymbol{e}_z \cdot [\boldsymbol{p} \times \hat{\boldsymbol{\sigma}}]$. In what follows, we make $\boldsymbol{k}_\parallel$ explicit only when necessary.

To obtain the wave functions in the junction, we first solve the BdG equation in each region. When a quasiparticle with the spin $\alpha = \uparrow$ or $\downarrow$ is injected into the interface, the wave function in the N region can be written as a linear combination of every possible wave functions:

$$\Psi^N(z) = e^{+ik_z^N \check{\tau}_3 z} \vec{a}_\alpha + e^{-ik_z^N \check{\tau}_3 z} \vec{r}_\alpha \tag{20}$$

$$\vec{a}_\alpha = \begin{cases} (\ 1\ \ 0\ \ 0\ \ 0\ )^T & \text{for } \alpha = \uparrow \\ (\ 0\ \ 1\ \ 0\ \ 0\ )^T & \text{for } \alpha = \downarrow \end{cases} \tag{21}$$

$$\vec{r}_\alpha = (\ r^p_{\uparrow\alpha} \quad r^p_{\downarrow\alpha} \quad r^h_{\uparrow\alpha} \quad r^h_{\downarrow\alpha}\ )^T, \tag{22}$$

where $r^{p(h)}_{\alpha'\alpha}$ is the normal (Andreev) reflection coefficients. The momentum in the z-direction is given by $k_z^N = \sqrt{2m_N \mu_{\boldsymbol{k}_\parallel}}/\hbar$ where we have used the Andreev approximation valid when $\mu \gg \Delta_0$, which allows us to ignore the energy dependence of the momentum. The wave function in the SC is given by

$$\Psi^S(z) = \check{U} e^{ik_z^S \check{\tau}_3 z} \vec{t}, \tag{23}$$

$$\check{U} = \begin{bmatrix} u_0 \hat{\sigma}_0 & v_0 \hat{\Delta}_o / d_{\boldsymbol{k}} \\ v_0 \hat{\Delta}_o^\dagger / d_{\boldsymbol{k}} & u_0 \hat{\sigma}_0 \end{bmatrix} \tag{24}$$

$$\vec{t}_\alpha = (\ t^p_{1\alpha},\ \ t^p_{2\alpha},\ \ t^h_{1\alpha},\ \ t^h_{2\alpha}\ )^T, \tag{25}$$

where we have used the Andreev approximation; $k_z^S = \sqrt{2m_z \mu_{k_\parallel}}/\hbar$. The $t^{p(h)}_{1(2)}$ coefficients are the transmission coefficients where the superscript indicates the transmission as a particle-like or hole-like quasiparticle and the subscript does the band index.

The differential conductance can be obtained from the reflection coefficients as in Blonder-Tinkham-Klapwijk (BTK) theory[62]. To obtain the reflection coefficients, we need to match the wave functions at the interface $z = 0$. There are two boundary conditions to conserve the probability density:

$$\Psi^N(z)\Big|_{z=0} = \Psi^S(z)\Big|_{z=0}, \tag{26}$$

$$\lim_{\gamma\to 0} \int_{-\gamma}^{\gamma} \check{H}\Psi(z) dz = \lim_{\gamma\to 0} \int_{-\gamma}^{\gamma} E\Psi(z) dz. \tag{27}$$

Substituting the wave function in each region, we obtain the first boundary condition in terms of the coefficients

$$\vec{a}_\alpha + \vec{r}_\alpha = \check{U} \vec{t}_\alpha, \tag{28}$$

and the second boundary condition

$$(\vec{a}_\alpha - \vec{r}_\alpha) - \check{V}_S \check{U} \vec{t} = 0, \tag{29}$$

$$\check{V}_S = \bar{v}_S \check{U}' \check{U}^{-1} + 2i\check{\tau}_3 \check{V}/\hbar v_N, \tag{30}$$

where $\check{U}' = \check{\tau}_3 \check{U} \check{\tau}_3$, $v_{N(S)} = \hbar k_z^{N(S)}/m_z$ are the velocities in the N (S), and $\bar{v}_S = v_S/v_N$. Combining the equations (28) and (29), we obtain the following equation

$$\vec{r}_\alpha = \left(\check{\tau}_0 + \check{V}_S\right)^{-1} \left(\check{\tau}_0 - \check{V}_S\right) \vec{a}_\alpha. \tag{31}$$

Calculating $\vec{r}_\alpha$ numerically, we can obtain the reflection coefficients for each reflection process.

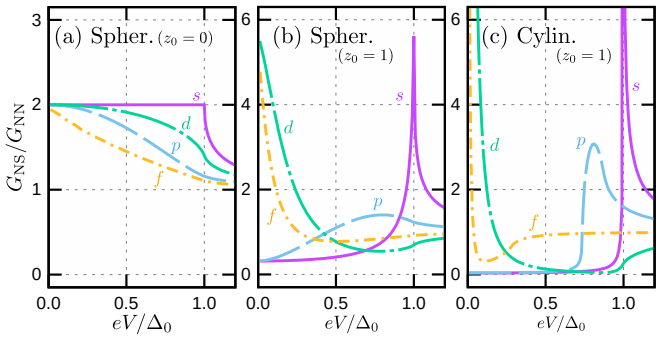

FIG. 3. Conductance of the NS junction along the c-axis. The indices s, p, d, and f means the SW, helical PW, chiral DW, and FW pairing respectively. The Fermi surface is spherical in (a) and (b), and cylindrical in (c). The normalized effective masses in (c) are set to $(\bar{m}_x, \bar{m}_y, \bar{m}_z) = (1.3, 1.3, 16.0)$. The barrier potential is set to $z_0 = 0$ in (a) and $z_0 = 1$ in (b) and (c). The conductance is normalized to its value in the normal state $G_{\rm NN}$. The result for chiral PW is the identical to that for helical PW in the absence of spin-dependent potentials.

The differential conductance $G(eV) = dI/dV$ can be calculated by BTK formula[62]. The conductance is give by

$$G(eV) = \sum_{\boldsymbol{k}_\parallel,\alpha} g_\alpha(E = eV, \boldsymbol{k}_\parallel)\Theta(\theta_s - \theta_c) \tag{32}$$

$$g_\alpha = v_N[1 - (\vec{r}_\alpha)^\dagger \check{\tau}_3 \vec{r}_\alpha], \tag{33}$$

where g_α is the partial conductance. In the cylindrical-FS model, we introduce the cut-off angle θ_c as shown in Fig. 2(a). When $\theta_s < \theta_c$ with $\tan\theta_s = k_\parallel/k_z^S$, the partial charge current cannot flow the junction. Throughout this paper, we consider the zero-temperature.

III. TUNNELLING SPECTROSCOPY ALONG c AXIS

The differential conductance along the c-axis is shown in Fig. 3. The conductance $G_{\rm NS}$ is normalized to its value in the normal state $G_{\rm NN}$, which is obtained by setting $\Delta_0 = 0$. The FS is spherical in Figs. 3(a) and 3(b) and cylindrical in Fig. 3(c), where the effective mass[15] is respectively set to $(\bar{m}_x, \bar{m}_y, \bar{m}_z) = (1.0, 1.0, 1.0)$ and $(1.3, 1.3, 16.0)$ with $\bar{m}_\nu = m_\nu/m_N$. The barrier potential is $z_0 = 0$ in Fig. 3(a) and $z_0 = 1.0$ in Figs. 3(b) and 3(c).

When the FS is spherical, $G_{\rm NS}$ without the barrier is larger than $G_{\rm NN}$ within the gap as shown in Fig. 3(a). In this case, the normal reflection is forbidden because there is no barrier and no Fermi-momentum mismatch. As a result, the injected quasiparticle within the gap propagates into the SC as a Cooper pair with the charge $2e$. Therefore, the conductance $G_{\rm NS}$ must be larger than $G_{\rm NN}$. In an unconventional SC, the gap size depends on $\boldsymbol{k}$ and can be smaller than Δ_0, which changes the conductance spectra depending on the node type. The helical PW has the point nodes at $k_a = k_b = 0$ and show the dome-shape $G_{\rm NS}$[15]. The chiral DW has a line node at $k_c = 0$ in addition to the point node. However, its gap amplitude $d_{\boldsymbol{k}}$ maximizes at $k_c/k_\perp^s = 1/\sqrt{2}$ which results in a larger $G_{\rm NS}$ than that of the helical PW case where $d_{\boldsymbol{k}}$ maximizes at $k_c = 0$ (i.e., at the velocity $v_N = 0$). The FW has line nodes at $k_a = 0$ and $k_b = 0$ which results in the sharper ZEP.

The barrier potential changes the conductance spectra drastically as shown in Fig. 3(b). The conductance for the chiral DW and FW junctions have sharp ZEPs due to the resonant tunneling through the zero-energy ABSs at the interface similar to in-plane tunneling of d_{xy}-wave[50] and p_x-wave junctions[63,64]. The pair potential of the chiral DW and FW SCs is antisymmetric under $k_c \leftrightarrow -k_c$ which results in the ABSs at the (001) surface[65]. In contrast, the conductance for the helical PW is V-shaped at the low energy reflecting the point node. The coherence peak around $|eV| \sim 0.7\Delta_0$ is broad because of the angle-dependent pair potential. The conductance spectra for the SW is well-known U-shaped one in the presence of the barrier potential.

When the FS in the SC is cylindrical, the node structure near $k_a = k_b = 0$ cannot contribute to the transport. Moreover, the channels relevant to the transport is restricted [see Fig. 2(a)]. Consequently, as indicated in Fig. 3(c), $G_{\rm NS}$ for the helical PW changes from V-shape to U-shape because the point node does not contribute to the transport. The characteristic energy scale for the FW is changed: a kink appears around $|eV| \sim 0.4\Delta_0$. In the FW junction, the channels with $d_{\boldsymbol{k}} = \Delta_0$ cannot contribute to the transport due to the cutoff for modelling the cylindrical FS of Sr_2RuO_4[66]. Therefore, the conductance structure appears only at $|eV| < 0.4\Delta_0$. The ZEPs for the chiral DW and FW becomes narrower than those for the spherical-FS case because the Fermi-momentum mismatch reduces the transparency at the interface.

A. Robust zero-energy peak of chiral d-wave junction

Near an N/SC interface, the parity mixing occurs due to the RSOI. To discuss the robustness of the zero-energy peak against parity mixing, we calculate $G_{\rm NS}$ taking into account the RSOI at the interface[13,15]. The RSOI at an interface changes $G_{\rm NS}$ significantly. For instance, it is demonstrated that the ZEP of spin-singlet chiral SCs are robust against the RSOI, whereas those of spin-triplet chiral SCs can be suppressed[67]. The effects of the RSOI on the conductance with the *spherical* FS are shown in Fig. 4, where $z_0 = 1$ and the pairing is assumed (a) FW, (b) chiral DW, and (c) helical PW pairings. The ZEP of the spin-singlet SC can survive even in the presence of the strong RSOI as shown in Fig. 4(a). In the present case, the ZEP of the triplet SC can survive even in the presence of the strong RSOI as shown in Fig. 4(b) because we consider a different situation from Ref. 67. In the

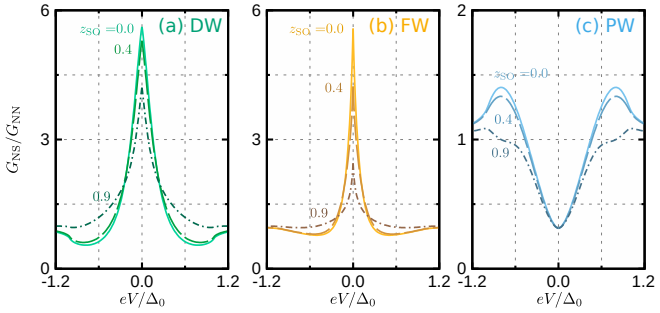

FIG. 4. Effects of Rashba spin-orbit interaction on the conductance along c-axis with *spherical* Fermi surface. The strength of the RSOI are set to $z_{SO} = 0$, 0.4, and 0.9. The barrier potential is set to $z_0 = 1$. The conductance is normalized to its value in the normal state G_{NN}.

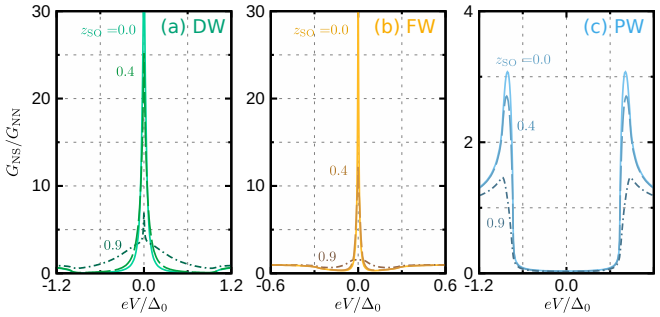

FIG. 5. Effects of Rashba spin-orbit interaction on the conductance with *cylindrical* Fermi surface. The results are plotted in the same manner as in Fig. 4. The parameters are set to the same values as the corresponding panels in Fig. 4.

present case, the d-vector is $\boldsymbol{d} \perp \boldsymbol{z}$, whereas $\boldsymbol{d} \parallel \boldsymbol{z}$ in their case. The coherence peak for the helical PW is suppressed by the ROSI as shown in Fig. 4(c).

When the FS is cylindrical, the channels with small $|\boldsymbol{k}_\parallel|$ cannot contribute to the transport [see Fig. 2(a)]. In other words, the charge current is mainly carried by the channels with the stronger RSOI whose amplitude is proportional to $|\boldsymbol{k}_\parallel|$. The conductance with the cylindrical FS is shown in Fig. 5. The ZEP for the spin-singlet chiral DW is robust against the RSOI, whereas that for the FW is fragile. Their peak heights at $z_{SO} = 0.9$ are $G_{NS}(eV = 0) \sim 7G_{NN}$ and $1.8G_{NN}$, respectively. The conductance of the helical PW junction does not qualitatively depend on the shape of the FS.

The angle-resolved zero-energy G_{NS} for the chiral DW and spin-nematic FW are respectively shown in Figs. 6(a) and 6(b), where $(\bar{m}_x, \bar{m}_y, \bar{m}_z) = (1.3, 1.3, 16.0)$, $z_0 = 3.0$, and $z_{SO} = 1.0$. The circles with the solid and broken line in Fig. 6 indicate the maximum $|\boldsymbol{k}_\parallel|$ in the N and the minimum $\boldsymbol{k}_\parallel$ in the SC due to the cutoff. In the cylindrical-FS model, only the channels between the solid and broken circles can contribute to G_{NS}. The zero-energy ABS for the chiral DW state is robust against the RSOI, while that for the FW one is substantially suppressed. This difference comes from the difference in

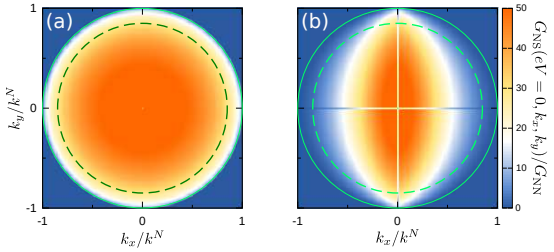

FIG. 6. Effects of Rashba spin-orbit interaction on angle-resolved zero-energy conductance of c-axis junction. The chiral DW and spin-nematic FW pairings are used in (a) and (b), respectively. The circles with the solid and broken line indicate the Fermi surface of the N and the smallest radius of the cylindrical Fermi surface in S. In the cylindrical-FS model, only the channels between solid and broken circles can contribute the conductance.

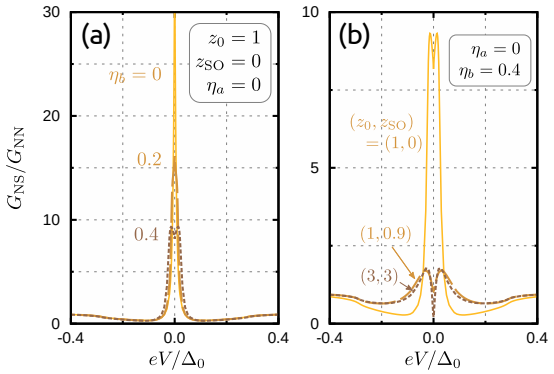

FIG. 7. Effects of the subdominant component $\boldsymbol{z}p_y$ on G_{NS} of the FW junction. A subdominant component is added to the FW pairing as given in Eq. (12). In the calculations, we set $\eta_a = 0$ and $\eta_b \neq 0$ reflecting the nematic superconducting state. The results for $\eta_a \neq 0$ and $\eta_b = 0$ are not qualitatively different from those shown in the figures above. The cylindrical FS is used. (a) The subdominant component splits the ZEP, where the parameters are set to $z_0 = 1$ and $z_{SO} = 0$. (b) When both of the subdominant component and the RSOI exist, G_{NS} can be even a narrow V-shaped one, where the parameters are set to $(z_0, z_{SO}) = (1, 0)$, $(1, 0.9)$, or $(3, 3)$

parity of these pairings: the chiral DW (spin-nematic FS) pairing is even (odd) under inversion. For an even-parity SC, a line node can be topologically stable and correspondingly a robust ABS with a flat band arises at an interface.[67] On the other hand, no topologically stable line node exists for an odd-parity SC with a spin-orbit interaction, and therefore a zero-energy ABS is fragile against the RSOI.

The fragility of the ZEP for the FW pairing is more prominent when taking into account the subdominant pairing state in Eq. (12). The effects of the subdominant component on G_{NS} of the FW junction are shown in Fig. 7, where the cylindrical FS is employed. In the calculations, we have used asymmetric parameter (i.e., $\eta_a = 0$ and $\eta_b \neq 0$) reflecting the nematic nature. The results with $\eta_a \neq 0$ and $\eta_b = 0$ are not qualitatively

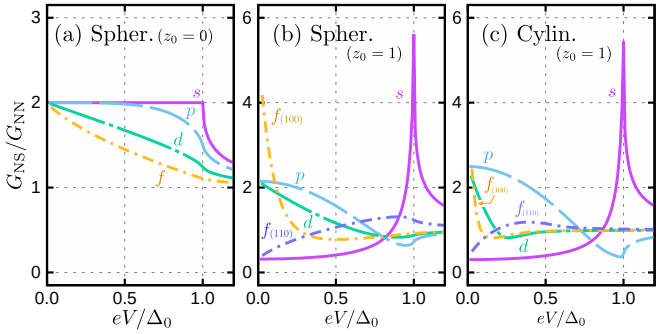

FIG. 8. Conductance of the NS junction with $\boldsymbol{c} \perp \boldsymbol{z}$. The results are plotted in the same manner as in Fig. 3. In the in-plane junction, $G_{\rm NS}$ for the FW SC depends on the direction of the interface; ZEP for (100) and V-shaped for (110).

different from those shown in this paper. As shown in Fig. 7(a), the ZEP is split and suppressed by the subdominant component even when $z_{\rm SO} = 0$. When both of the subdominant component and the RSOI exist, the low-energy spectrum can be V-shaped even though the width of the structure is narrower than Δ_0 as shown in Fig. 7(b), where $\eta_b = 0.4$ and $(z_0, z_{\rm SO}) = (1, 0)$, $(1, 0.9)$, or $(3, 3)$.

So far, ABSs have never been experimentally observed in the (001) surface of Sr_2RuO_4[58–60]. Therefore, we conclude that the $d_{zx}+id_{yz}$-wave does not explain the transport measurements along the c-axis of Sr_2RuO_4. The spin-nematic FW and helical PW pairings remain as possible pairing symmetry of Sr_2RuO_4.

IV. IN-PLANE TUNNELING SPECTROSCOPY

The in-plane tunneling spectroscopy can distinguish the spin-nematic FW and helical PW without ambiguity. The results are shown in Fig. 8. The parameters are set to (a) $(z_0, \bar{m}_x, \bar{m}_y, \bar{m}_z) = (0, 1, 1, 1)$, (b) $(1, 1, 1, 1)$, and (c) $(1, 1.3, 16, 1.3)$. In the absence of z_0, the conductance $G_{\rm NS}$ for the helical PW, chiral DW, and FW are dome-shaped ZEP, ZEP, and ZEP, respectively. When $z_0 \neq 0$, $G_{\rm NS}$ shows different behavior depending on the pairing symmetry. In particular, $G_{\rm NS}$ for the FW significantly depends on the direction of the junction. As shown in Fig. 8(b), $G_{\rm NS}$ for the FW are the ZEP or V-shaped dip in the (100) and (110) junctions, respectively. In the helical PW and chiral DW junctions, $G_{\rm NS}$ do not depend on the direction of the junction[68] as in the chiral p-wave junction[53]: both of them show the broad ZEP. Comparing Figs. 8(b) and 8(c), we see that the shape of the FS in the SC does not change $G_{\rm NS}$ qualitatively in the in-plane junction. Note that, when the FS is cylindrical, the characteristic energy scale for chiral DW and FW are smaller than those for helical PW and SW because the channels with $d_{\boldsymbol{k}} = \Delta_0$ cannot contribute the transport in the chiral DW and FW cases [see Fig. 2(b)].

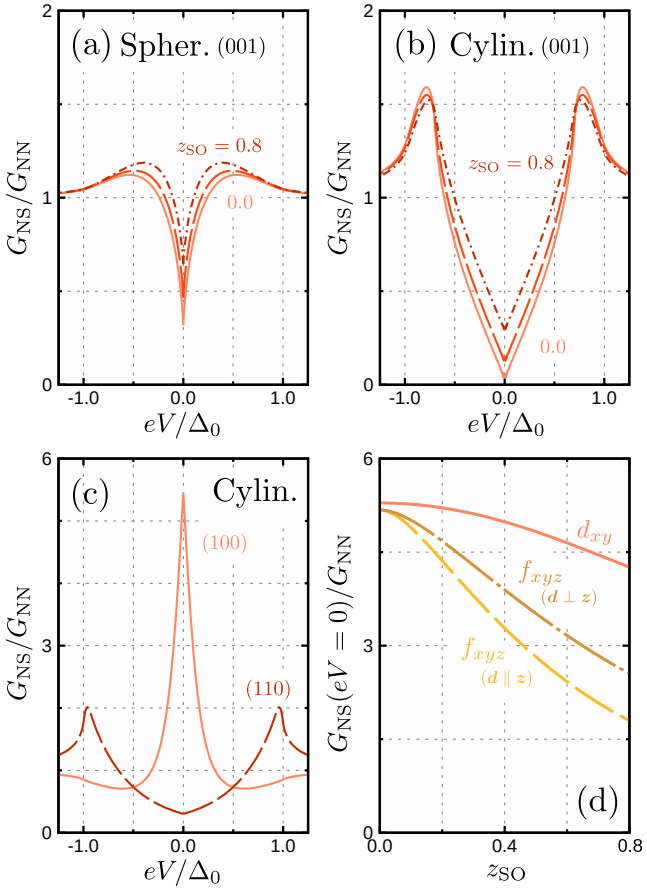

FIG. 9. (a)(b) Conductance of the *non-chiral* d-wave junction with $\boldsymbol{c} \parallel \boldsymbol{z}$. The width of the V-shaped is characterized by Δ_0. (c) Conductance of the *non-chiral* d-wave junction with $\boldsymbol{c} \perp \boldsymbol{z}$. (d) $z_{\rm SO}$-dependences of $G_{\rm NS}|_{eV=0}$ for $d_{xy}-$ and f_{xyz}-wave pairings. The zero-energy peak for d_{xy}-wave junction is more robust against spin mixing than those for f-wave. The barrier parameters are set to $z_0 = 1$ in (a), (b), (c), and (d). The spin-orbit interaction is set to $z_{\rm SO} = 0.0$, 0.6, and 0.8 in (a) and (b), and $z_{\rm SO} = 0.0$ in (c).

V. SPIN-NEMATIC f-WAVE VERSUS NON-CHIRAL d_{xy}-WAVE

The comparison between the spin-nematic f_{xyz}-wave and spin-singlet *non-chiral* d_{xy}-wave pairings would provide useful information to discuss the pairing symmetry of Sr_2RuO_4 even though the non-chiral d_{xy}-wave pairing did not explain several experiments. The conductance spectra $G_{\rm NS}$ of the d_{xy}-wave junction are known to be similar to those of the FW junction: $G_{\rm NS}$ shows the V-shaped, ZEP, and V-shaped spectra in the (001)-, (100)-, and (110)-interface junctions.

The conductance spectra along the c-axis of the *non-chiral* d-wave junctions are shown in Fig. 9(a) and 9(b), where the spherical and cylindrical FS is used in Fig. 9(a) and 9(b) respectively and the d_{xy}-wave pair potential is given by $d_0 = \bar{\Delta}_0(\partial_a\partial_b)/(k_\parallel^S)^2$. In both cases, $G_{\rm NS}$ is V-shaped regardless of $z_{\rm SO}$. Differing from the FW case in

TABLE I. Summary of conductance spectra. The spectra strongly depends on the paring symmetry and the direction of the junction. The conductance spectra are classified into three types: zero-energy peak (ZEP), dome-like broad peak (Dome), U-shaped dip (U), and V-shaped dip (V). The helical PW is consistent with the NMR measurements only qualitatively but not quantitatively.

		c axis	ab plane (100)	ab plane (110)	NMR	TRS	Node Horiz.	Node Vert.	Irr. rep.
$p_x + ip_y$	$\boldsymbol{e}_c(k_a + ik_b)$	U	Dome		No	No	No		2D
Helical p	$\boldsymbol{e}_a k_a + \boldsymbol{e}_b k_b$	U	Dome		"Yes"	Yes	No		1D
$d_{zx} + id_{yz}$	$(k_a + ik_b)k_c$	ZEP	ZEP		Yes	No	Yes	No	2D
Nematic f_{xyz}	$\boldsymbol{e}_a(k_a k_b k_c)$	ZEP or V	ZEP	V	Yes	Yes	Yes	Yes	2D
d_{xy}	$k_a k_b$	V	ZEP	V	Yes	Yes	No	Yes	1D

Fig. 7(b), the width of the V-shaped structure is about Δ_0 in the d_{xy}-wave case. The V-shaped structure is more prominent in the cylindrical-FS model [i.e., Fig. 9(b)] because channels near the intersection of the two line nodes ($k_x = k_y = 0$) do not contribute to the transport because of the cutoff θ_c.

The conductance spectra of in-plane junctions (i.e., $\boldsymbol{c} \perp \boldsymbol{z}$) are shown in Fig. 9(c). The transport in this case have been established[69]: $G_{\rm NS}$ becomes ZEP and V-shaped in the (100)- and (110)-interface junctions respectively. The $z_{\rm SO}$-dependences of $G_{\rm NS}|_{eV=0}$ for the d_{xy}- and spin-nematic f_{xyz}-wave pairings are shown in Fig. 9(d), where d-vector for the FW is assumed $\boldsymbol{d} \parallel \boldsymbol{a}$ or $\boldsymbol{d} \parallel \boldsymbol{b}$. The ZEP for the d_{xy} is more robust against the spin-mixing than those of f_{xyz}-wave junctions as shown in Fig. 9(d).

VI. DISCUSSIONS

The conductance spectra for each pairing and each junction direction are summarized in Table I, where the conductance spectra are classified into the four types: zero-energy peak (ZEP), dome-like broad peak (Dome), U-shaped dip (U), and V-shaped dip (V). The tunneling spectroscopy of the (001)-, (100)-, and (110)-interface junctions is found to be important clues to identify the pairing symmetry of Sr_2RuO_4. In particular, it should be emphasized that the c-axis transport measurements by the STM[58–60] are inconsistent with the chiral DW scenario, but support both of the spin-nematic FW and helical PW. These pairings can clearly be distinguished by transport measurements of the (100) and (110) junctions. Such a direction-dependent $G_{\rm NS}$ has been well established for high-T_c d-wave SCs. In the high-T_c SC, the ZEP appears in the (110) junction and does not in the (100) junction[50,70,71].

We did not take multiband effects into account. However, the multiband effect does not change $G_{\rm NS}$ qualitatively but quantitatively[72]. In particular, for the (001) junction, the interaction among the bands would not play a substantial role in transport in the [001] direction since the energy bands are less dispersive with respect to k_c and do not overlap each other when they are projected in the k_a-k_b plane. The conductance spectra in in-plane junctions, would be modified by the multiband effects more significantly compared with those of the (001) junction. However, the conductance spectra in the [100] and [110] directions for the helical PW (spin-nematic FW) pairing are expected to be *qualitatively* identical (different) because the multiband effects change the spectra only qualitatively. It would be interesting to calculate $G_{\rm NS}$ of the chiral d-wave, helical p-wave, and spin-nematic f_{xyz}-wave junctions with taking the multiband effect into account.

The spatial dependence of the pair potential, which is caused by the surface reconstruction, the interface reflection[34,35,73,74], and interface roughness[41,42,75,76], is not taken into account in the present calculations. The spatial dependence would change $G_{\rm NS}$ quantitatively but not qualitatively. Therefore, our conclusion would be valid even if the pair potential is spatial dependent.

VII. SUMMARY

In this paper, we have proposed that the tunneling spectroscopy of three-dimensional normal-metal/Sr_2RuO_4 junctions enables to determine the pairing symmetry of Sr_2RuO_4. The differential conductances in the [001], [100], and [110] direction have been obtained by the Blonder-Tinkham-Klapwijk theory. We have considered three possible pairings, the spin-singlet $d_{zx} + id_{yz}$-wave, the spin-triplet helical p-wave, and the spin-nematic f_{xyz}-wave pairings, which are consistent with the NMR measurements. Introducing the anisotropic effective-mass and the cutoff in the momentum integration, the γ band of Sr_2RuO_4 is modeled.

Although the conductance spectra $G_{\rm NS}$ along the c-axis for the chiral $d_{zx} + id_{yz}$-wave and f_{xyz}-wave are similar when there is no spin-mixing (e.g., RSOI and the

subdominant pair potential), the spectra is significantly modified by the spin-mixing depending on the pairing symmetry: $G_{\rm NS}$ for the $d_{zx}+id_{yz}$-wave is not qualitatively changed by the spin-mixing, whereas the ZEP in the $G_{\rm NS}$ for the spin-nematic f_{xyz}-wave is strongly suppressed. Comparing the calculated $G_{\rm NS}$ and the corresponding transport experiments, we have concluded the spin-singlet $d_{zx}+id_{yz}$-wave scenario does not explain the STM experiments, whereas the spin-nematic f_{xyz}-wave and helical PW pairings do.

We have also proposed that these two remaining candidates can be distinguished without ambiguity by the in-plane Andreev spectroscopy. The conductance spectra for the spin-nematic f_{xyz}-wave support a ZEP and a V-shaped dip in the (100)- and (110)-interface junctions respectively, whereas those of the helical p-wave junction are independent of the direction.

ACKNOWLEDGMENTS

The authors would like to thank S. Kashiwaya and S. Kobayashi for useful discussions. S.-I. S. is supported by Grant-in-Aid for JSPS Fellows (JSPS KAKENHI Grant Number JP19J02005). This work was supported by Grants-in-Aid from JSPS for Scientific Research on Innovative Areas "Topological Materials Science" (KAKENHI Grant Numbers JP15H05851, JP15H05853, JP15H05855, and JP15K21717), for Scientific Research (B) (KAKENHI Grant Number JP18H01176 and JP17H02922), Japan-RFBR Bilateral Joint Research Projects/Seminars number 19-52-50026, and JSPS Core-to-Core Program (A. Advanced Research Networks). This work was supported by JST CREST (No: JPMJCR19T2), Japan.

[1] Y. Maeno, H. Hashimoto, K. Yoshida, S. Nishizaki, T. Fujita, J. Bednorz, and F. Lichtenberg, Nature **372**, 532 (1994).
[2] A. P. Mackenzie and Y. Maeno, Rev. Mod. Phys. **75**, 657 (2003).
[3] Y. Maeno, S. Kittaka, T. Nomura, S. Yonezawa, and K. Ishida, J. Phys. Soc. Jpn. **81**, 011009 (2012).
[4] T. M. Rice and M. Sigrist, J. Phys.: Condens. Matter **7**, L643 (1995).
[5] J. A. Duffy, S. M. Hayden, Y. Maeno, Z. Mao, J. Kulda, and G. J. McIntyre, Phys. Rev. Lett. **85**, 5412 (2000).
[6] J. Jang, D. Ferguson, V. Vakaryuk, R. Budakian, S. Chung, P. Goldbart, and Y. Maeno, Science **331**, 186 (2011).
[7] Y. Yasui, K. Lahabi, M. S. Anwar, Y. Nakamura, S. Yonezawa, T. Terashima, J. Aarts, and Y. Maeno, Phys. Rev. B **96**, 180507(R) (2017).
[8] F. Laube, G. Goll, H. v. Löhneysen, M. Fogelström, and F. Lichtenberg, Phys. Rev. Lett. **84**, 1595 (2000).
[9] S. Kashiwaya, H. Kashiwaya, H. Kambara, T. Furuta, H. Yaguchi, Y. Tanaka, and Y. Maeno, Phys. Rev. Lett. **107**, 077003 (2011).
[10] M. Yamashiro, Y. Tanaka, and S. Kashiwaya, J. Phys. Soc. Jpn. **67**, 3364 (1998).
[11] R. Jin, Y. Zadorozhny, Y. Liu, D. G. Schlom, Y. Mori, and Y. Maeno, Phys. Rev. B **59**, 4433 (1999).
[12] Y. Tanaka, T. Yokoyama, A. V. Balatsky, and N. Nagaosa, Phys. Rev. B **79**, 060505(R) (2009).
[13] S. Wu and K. V. Samokhin, Phys. Rev. B **81**, 214506 (2010).
[14] M. Anwar, S. Lee, R. Ishiguro, Y. Sugimoto, Y. Tano, S. Kang, Y. Shin, S. Yonezawa, D. Manske, H. Takayanagi, et al., Nat. Commun. **7**, 13220 (2016).
[15] L. A. B. Olde Olthof, S.-I. Suzuki, A. A. Golubov, M. Kunieda, S. Yonezawa, Y. Maeno, and Y. Tanaka, Phys. Rev. B **98**, 014508 (2018).
[16] K. Ishida, H. Mukuda, Y. Kitaoka, K. Asayama, Z. Mao, Y. Mori, and Y. Maeno, Nature **396**, 658 (1998).
[17] T. Nomura and K. Yamada, J. Phys. Soc. Jpn. **69**, 3678 (2000). *Ibid.* **71**, 404 (2002). *Ibid.* **71**, 1993 (2002). *Ibid.* **74**, 1818 (2004).
[18] T. Nomura, D. S. Hirashima, and K. Yamada, J. Phys. Soc. Jpn. **77**, 024701 (2008).
[19] Y. Yanase and M. Ogata, J. Phys. Soc. Jpn. **72**, 673 (2003).
[20] S. Raghu, A. Kapitulnik, and S. A. Kivelson, Phys. Rev. Lett. **105**, 136401 (2010).
[21] M. Sato and M. Kohmoto, J. Phys. Soc. Jpn. **69**, 3505.
[22] K. Kuroki, M. Ogata, R. Arita, and H. Aoki, Phys. Rev. B **63**, 060506 (2001).
[23] T. Takimoto, Phys. Rev. B **62**, R14641 (2000).
[24] M. Tsuchiizu, Y. Yamakawa, S. Onari, Y. Ohno, and H. Kontani, Phys. Rev. B **91**, 155103 (2015).
[25] A. Pustogow, Y. Luo, A. Chronister, Y.-S. Su, D. Sokolov, F. Jerzembeck, A. Mackenzie, C. Hicks, N. Kikugawa, S. Raghu, et al., Nature **574**, 72 (2019).
[26] K. Ishida, M. Manago, and Y. Maeno, arXiv:1907.12236 (2019).
[27] S. Yonezawa, T. Kajikawa, and Y. Maeno, Phys. Rev. Lett. **110**, 077003 (2013).
[28] S. Yonezawa, T. Kajikawa, and Y. Maeno, J. Phys. Soc. Jpn. **83**, 083706 (2014).
[29] S. Kittaka, A. Kasahara, T. Sakakibara, D. Shibata, S. Yonezawa, Y. Maeno, K. Tenya, and K. Machida, Phys. Rev. B **90**, 220502 (2014).
[30] G. M. Luke, Y. Fudamoto, K. Kojima, M. Larkin, J. Merrin, B. Nachumi, Y. Uemura, Y. Maeno, Z. Mao, Y. Mori, et al., Nature **394**, 558 (1998).
[31] J. Xia, Y. Maeno, P. T. Beyersdorf, M. M. Fejer, and A. Kapitulnik, Phys. Rev. Lett. **97**, 167002 (2006).
[32] C. Lupien, W. A. MacFarlane, C. Proust, L. Taillefer, Z. Q. Mao, and Y. Maeno, Phys. Rev. Lett. **86**, 5986 (2001).
[33] N. Okuda, T. Suzuki, Z. Mao, Y. Maeno, and T. Fujita, J. Phys. Soc. Jpn. **71**, 1134 (2002).
[34] M. Matsumoto and M. Sigrist, J. Phys. Soc. Jpn. **68**, 994 (1999).
[35] A. Furusaki, M. Matsumoto, and M. Sigrist, Phys. Rev. B **64**, 054514 (2001).
[36] P. G. Björnsson, Y. Maeno, M. E. Huber, and K. A. Moler, Phys. Rev. B **72**, 012504 (2005).
[37] J. R. Kirtley, C. Kallin, C. W. Hicks, E.-A. Kim, Y. Liu, K. A. Moler, Y. Maeno, and K. D. Nelson, Phys. Rev. B **76**, 014526 (2007).

[38] C. W. Hicks, J. R. Kirtley, T. M. Lippman, N. C. Koshnick, M. E. Huber, Y. Maeno, W. M. Yuhasz, M. B. Maple, and K. A. Moler, Phys. Rev. B **81**, 214501 (2010).
[39] C. Kallin, Reports on Progress in Physics **75**, 042501 (2012).
[40] P. J. Curran, S. J. Bending, W. M. Desoky, A. S. Gibbs, S. L. Lee, and A. P. Mackenzie, Phys. Rev. B **89**, 144504 (2014).
[41] S.-I. Suzuki and Y. Asano, Phys. Rev. B **94**, 155302 (2016).
[42] S. V. Bakurskiy, N. V. Klenov, I. I. Soloviev, M. Y. Kupriyanov, and A. A. Golubov, Supercond. Sci. Technol. **30**, 044005 (2017).
[43] K. Kawai, K. Yada, Y. Tanaka, Y. Asano, A. A. Golubov, and S. Kashiwaya, Phys. Rev. B **95**, 174518 (2017).
[44] S. Kashiwaya, K. Saitoh, H. Kashiwaya, M. Koyanagi, M. Sato, K. Yada, Y. Tanaka, and Y. Maeno, Phys. Rev. B **100**, 094530 (2019).
[45] E. Hassinger, P. Bourgeois-Hope, H. Taniguchi, S. René de Cotret, G. Grissonnanche, M. S. Anwar, Y. Maeno, N. Doiron-Leyraud, and L. Taillefer, Phys. Rev. X **7**, 011032 (2017).
[46] S. Kittaka, S. Nakamura, T. Sakakibara, N. Kikugawa, T. Terashima, S. Uji, D. A. Sokolov, A. P. Mackenzie, K. Irie, Y. Tsutsumi, et al., J. Phys. Soc. Jpn. **87**, 093703 (2018).
[47] I. Žutić and I. Mazin, Phys. Rev. Lett. **95**, 217004 (2005).
[48] J. Hara and K. Nagai, Progress of Theoretical Physics **76**, 1237 (1986).
[49] C. Bruder, Phys. Rev. B **41**, 4017 (1990).
[50] Y. Tanaka and S. Kashiwaya, Phys. Rev. Lett. **74**, 3451 (1995).
[51] L. J. Buchholtz and G. Zwicknagl, Phys. Rev. B **23**, 5788 (1981).
[52] M. Yamashiro, Y. Tanaka, and S. Kashiwaya, Phys. Rev. B **56**, 7847 (1997).
[53] C. Honerkamp and M. Sigrist, J. Low Temp. Phys. **111**, 895 (1998).
[54] C. R. Hu, Phys. Rev. Lett. **72**, 1526 (1994).
[55] S. Kashiwaya and Y. Tanaka, Rep. Prog. Phys. **63**, 1641 (2000).
[56] T. Löfwander, V. S. Shumeiko, and G. Wendin, Supercond. Sci. Technol. **14**, R53 (2001).
[57] Y. Asano, Y. Tanaka, and S. Kashiwaya, Phys. Rev. B **69**, 134501 (2004).
[58] H. Suderow, V. Crespo, I. Guillamon, S. Vieira, F. Servant, P. Lejay, J. P. Brison, and J. Flouquet, New Journal of Physics **11**, 093004 (2009).
[59] I. A. Firmo, S. Lederer, C. Lupien, A. P. Mackenzie, J. C. Davis, and S. A. Kivelson, Phys. Rev. B **88**, 134521 (2013).
[60] R. Sharma, S. D. Edkins, Z. Wang, A. Kostin, C. Sow, Y. Maeno, A. P. Mackenzie, J. Davis, and V. Madhavan, arXiv preprint arXiv:1912.02798 (2019).
[61] In this paper, we consider subdominant component only for the FW pairing. Subdominant components in a spin-triplet superconductor can change the direction of the d-vector, resulting in the mixing between spin subspace. Such spin mixing can affects the surface ABSs.
[62] G. E. Blonder, M. Tinkham, and T. M. Klapwijk, Phys. Rev. B **25**, 4515 (1982).
[63] M. Yamashiro, Y. Tanaka, Y. Tanuma, and S. Kashiwaya, J. Phys. Soc. Jpn. **67**, 3224 (1998).
[64] H. Kwon, K. Sengupta, and V. Yakovenko, Eur. Phys. J. B **37**, 349 (2004).
[65] The ABSs are formed by the interference between the quasiparticles propagating with k_z and $-k_z$. The ABSs are present when the phases of the pair potentials $\Delta(\boldsymbol{k}_\parallel, k_z)$ and $\Delta(\boldsymbol{k}_\parallel, -k_z)$ are different. In particular, the ABS appears at the zero energy when the condition $\phi(\boldsymbol{k}_\parallel, k_z) - \phi(\boldsymbol{k}_\parallel, k_z) = \pi$ is satisfied, where ϕ is the phase of the pair potential[50,54–56].
[66] The energy scale depends also on the size of the FS in the N region.
[67] S. Kobayashi, Y. Tanaka, and M. Sato, Phys. Rev. B **92**, 214514 (2015).
[68] In the square-lattice tight-binding model, $G_{\rm NS}$ depends on the direction reflecting the FS anisotropy in the ab plane.
[69] Y. Tanaka and S. Kashiwaya, Phys. Rev. Lett. **74**, 3451 (1995).
[70] L. Alff, H. Takashima, S. Kashiwaya, N. Terada, H. Ihara, Y. Tanaka, M. Koyanagi, and K. Kajimura, Phys. Rev. B **55**, R14757 (1997).
[71] J. Y. T. Wei, N.-C. Yeh, D. F. Garrigus, and M. Strasik, Phys. Rev. Lett. **81**, 2542 (1998).
[72] K. Yada, A. A. Golubov, Y. Tanaka, and S. Kashiwaya, J. Phys. Soc. Jpn. **83**, 074706 (2014).
[73] Y. Barash, A. Svidzinsky, and H. Burkhardt, Phys. Rev. B **55**, 15282 (1997).
[74] Y. Nagato, K. Nagai, and J. Hara, J. Low Temp. Phys. **93**, 33 (1993).
[75] Y. Nagato, M. Yamamoto, and K. Nagai, J. Low Temp. Phys. **110**, 1135 (1998).
[76] Y. Tanuma, Y. Tanaka, and S. Kashiwaya, Phys. Rev. B **64**, 214519 (2001).